Monthly Notices of the ROYAL ASTRONOMICAL SOCIETY

MNRAS **540,** 3677–3692 (2025) https://doi.org/10.1093/mnras/staf894
Advance Access publication 2025 June 03

JWST NIRISS transmission spectroscopy of the super-Earth GJ 357b, a favourable target for atmospheric retention

Jake Taylor [1]★ Michael Radica [2,3]† Richard D. Chatterjee [1] Mark Hammond [1] Tobias Meier [1] Suzanne Aigrain [1] Ryan J. MacDonald [4] Loic Albert [3] Björn Benneke [3] Louis-Philippe Coulombe [3] Nicolas B. Cowan [5,6] Lisa Dang [3] René Doyon [3] Laura Flagg [7] Doug Johnstone [8,9] Lisa Kaltenegger [10] David Lafrenière [3] Stefan Pelletier [3,11] Caroline Piaulet-Ghorayeb [2,3]‡ Jason F. Rowe [12] and Pierre-Alexis Roy [3]

[1]*Department of Physics, University of Oxford, Parks Rd, Oxford OX1 3PU, UK*
[2]*Department of Astronomy & Astrophysics, University of Chicago, 5640 South Ellis Avenue, Chicago, IL 60637, USA*
[3]*Trottier Institute for Research on Exoplanets, Université de Montréal, 1375 Avenue Thérèse-Lavoie-Roux, Montréal, QC H2V 0B3, Canada*
[4]*Department of Astronomy, University of Michigan, 1085 South University Avenue, Ann Arbor, MI 48109, USA*
[5]*Department of Physics, McGill University, 3600 University St, Montreal, QC H3A 2T8, Canada*
[6]*Department of Earth & Planetary Sciences, McGill University, 3450 University St, Montréal, H3A 2A7, Canada*
[7]*Department of Physics and Astronomy, Johns Hopkins University, Baltimore, MD, 21218, USA*
[8]*NRC Herzberg Astronomy and Astrophysics, 5071 West Saanich Rd, Victoria, BC V9E 2E7, Canada*
[9]*Department of Physics and Astronomy, University of Victoria, Victoria, BC V8P 5C2, Canada*
[10]*Astronomy Department, Cornell University, Ithaca, NY 14853, USA*
[11]*Observatoire astronomique de l'Université de Genève, 51 chemin Pegasi 1290 Versoix, Switzerland*
[12]*Department of Physics and Astronomy, Bishops University, 2600 Rue College, Sherbrooke, QC J1M 1Z7, Canada*

Accepted 2025 May 30. Received 2025 May 28; in original form 2025 January 13

ABSTRACT

We present a *JWST* Near Infrared Imager and Slitless Spectrograph/Single Object Slitless Spectroscopy transmission spectrum of the super-Earth GJ 357 b: the first atmospheric observation of this exoplanet. Despite missing the first ∼40 per cent of the transit due to using an out-of-date ephemeris, we still recover a transmission spectrum that does not display any clear signs of atmospheric features. We perform a search for Gaussian-shaped absorption features within the data but find that this analysis yields comparable fits to the observations as a flat line. We compare the transmission spectrum to a grid of atmosphere models and reject, to 3σ confidence, atmospheres with metallicities $\lesssim 100\times$ solar (∼4 g mol^{-1}) with clouds at pressures down to 0.01 bar. We analyse how the retention of a secondary atmosphere on GJ 357 b may be possible due to its higher escape velocity compared to an Earth-sized planet and the exceptional inactivity of its host star relative to other M2.5V stars. The star's XUV luminosity decays below the threshold for rapid atmospheric escape early enough that the volcanic revival of an atmosphere of several bars of CO_2 is plausible, though subject to considerable uncertainty. Finally, we model the feasibility of detecting an atmosphere on GJ 357 b with MIRI/LRS, MIRI photometry, and NIRSpec/G395H. We find that, with two eclipses, it would be possible to detect features indicative of an atmosphere or surface. Further to this, with three to four transits, it would be possible to detect a 1 bar nitrogen-rich atmosphere with 1000 ppm of CO_2.

Key words: planets and satellites: atmospheres – planets and satellites: individual: GJ 357 b – planets and satellites: terrestrial planets.

1 INTRODUCTION

The search for atmospheres around terrestrial exoplanets is a key science goal of the *JWST*. To date, there have been an array of observations, in both transmission and emission, attempting to detect atmospheres around terrestrial worlds, but none have yet been fruitful. To first order, the key limitation with determining the presence of an atmosphere around a terrestrial planet is the small size of the planet versus the star. For larger stars, like the Sun, terrestrial planets will have a smaller planet-to-star radius ratio, and therefore a smaller observed transit depth, compared to those orbiting an M-dwarf. This has led to the emergence of the M-dwarf opportunity (Dressing & Charbonneau 2015) – that terrestrial planets around M-

★ E-mail: jake.taylor@physics.ox.ac.uk
† NSERC Post-doctoral Fellow.
‡ E. Margaret Burbridge Post-doctoral Fellow.

dwarfs are more favourable for atmosphere detection. Moreover, due to their lower luminosity compared to Sun-like stars, the habitable zones around M-dwarfs are located at shorter orbital periods. This makes habitable zone planets around M-dwarfs more likely to transit, and more amenable to repeated atmosphere observations.

Despite the above benefits for potential detections of terrestrial planet atmospheres, M-dwarf stars also pose significant challenges for this endeavour. Interactions between a star's coronal plasma and dynamo-induced magnetic field generates ionizing radiation. Since low-mass stars spin-down more slowly than Sun-like ones, their ratio of ionizing to bolometric luminosity remains at a maximum for much longer, up to billions of years, and generally remains higher at all ages (Johnstone, Bartel & Güdel 2021). The raised fluxes of ionizing radiation to which M-dwarfs expose their companion rocky planets can be effective in evaporating primordial hydrogen (e.g. Ho et al. 2024) and the volcanic atmospheres that may follow (e.g. Chatterjee & Pierrehumbert 2024). Thus, the sweet spot for observing rocky planet atmospheres is around relatively inactive M-dwarfs, which generally means those that started rotating relatively slowly at birth.

Furthermore, the generally high activity levels of M-dwarfs during their main-sequence phase leads to high occurrence rates of photosphere heterogeneities (i.e. spots and faculae on the stellar surface). If occulted during a planet transit, these heterogeneities can contaminate observed light curves (e.g. Fournier-Tondreau et al. 2024). Though, the more problematic scenario is when heterogeneities remain unocculted, in which case they can directly bias transmission spectra themselves via the transit light source (TLS) effect (Pont et al. 2008; Rackham, Apai & Giampapa 2018, 2019; Lim et al. 2023; Cadieux et al. 2024; Radica et al. 2025). Moreover, particularly for late-type M-dwarfs, photosphere temperatures are low enough that H_2O can condense in their star-spots. This can result in H_2O spectral features being imprinted on an orbiting planet's transmission spectrum via the TLS effect – potentially spoofing the presence of an atmosphere on the planet itself.

Theoretical models have predicted that short-period terrestrial planets with radii $\lesssim 1.4\,R_\oplus$ should not retain atmospheres that are rich in H_2/He (Rogers et al. 2021). Evidence of a lack of H/He dominated atmospheres around rocky planets was mounting already in the pre-*JWST* era. For example, observations of the TRAPPIST-1 system (e.g. de Wit et al. 2016, 2018; Wakeford et al. 2019; Garcia et al. 2022; Zhou et al. 2023) and the L98-59 system (e.g. Damiano et al. 2022; Zhou et al. 2023) were able to rule out H/He rich atmospheres; however these observations did not have the precision to distinguish between high-mean-molecular-weight atmospheres, clouds, or airlessness. Now, with the unprecedented precision and wavelength coverage of *JWST*, a new era has begun for the detection and characterization of atmospheres around small, rocky planets.

The exoplanet community commonly uses the cosmic shoreline as a rule of thumb (Zahnle & Catling 2017; Redfield et al. 2024) – an empirically motivated boundary distinguishing planets with and without atmospheres based on their instellation and escape velocity. However, the photoevaporation cosmic shoreline does not differentiate between primary and secondary atmospheres or between early and main-sequence escape, implying that planets traditionally classified as airless may, in fact, have evolved to retain atmospheres. One such evolutionary pathway is the volcanic revival of an atmosphere from a bare rock, a scenario that has received little attention since Kite & Barnett (2020). Stellar ionizing luminosity typically declines more rapidly than exoplanetary mantles are thought to deplete and determining whether volatile supply can then outpace atmospheric loss depends on the non-linear physics of escape, mantle evolution, and stellar variability (e.g. Dorn, Noack & Rozel 2018; France et al. 2020; Nakayama, Ikoma & Terada 2022).

1.1 Overview of *JWST* transit observations of rocky planets

As outlined above, probing for atmospheres of terrestrial planets has been one of the main science objectives of *JWST* over the first few cycles, and numerous such programmes have been carried out, both via transit and eclipse observations. Transit programmes using NIRSpec/G395H (3–5 μm), primarily aiming to detect the signatures of CO_2 at 4.3 μm have been published for six planets: TOI-836 b (Alderson et al. 2024), L 98-59 c (Scarsdale et al. 2024), L 168-9 c (Alam et al. 2024), LHS 457 b (Lustig-Yaeger et al. 2023), GJ 486 b (Moran et al. 2023), and GJ 1132 b (May et al. 2023). All of these analyses were able to rule out cloud-free, H_2/He-dominated atmospheres, but were unable to definitively rule on the presence of a secondary atmosphere due to the flatness of the observed transmission spectrum (Lustig-Yaeger et al. 2023; Alam et al. 2024; Alderson et al. 2024; Scarsdale et al. 2024), or the degenerate effects of TLS (May et al. 2023; Moran et al. 2023). However, follow-up MIRI/LRS (5–12 μm) eclipse observations of GJ 486 b suggest that the planet is indeed airless (Mansfield et al. 2024).

Transit observations of GJ 341 b with NIRCam/*F444W* (3.9–5 μm) by Kirk et al. (2024) also yield a similar conclusion. While NIRCam transit spectra of L 98–59 d by Gressier et al. (2024a) and Banerjee et al. (2024) yield tentative evidence of atmospheric features – the significance of these depended heavily on the particular data reduction and light curve fitting.

Finally, the two inner planets of the TRAPPIST-1 system (Gillon et al. 2016, 2017) have been observed in transit with Near Infrared Imager and Slitless Spectrograph/Single Object Slitless Spectroscopy (NIRISS/SOSS) (0.6–2.8 μm) and in eclipse using MIRI photometry by Lim et al. (2023) and Greene et al. (2023), respectively for planet b, and Radica et al. (2025) and Zieba et al. (2023), respectively for planet c. In both cases, the NIRISS/SOSS observations were dominated by stellar contamination, whereas the MIRI eclipses were consistent with the planets being airless bodies. It should be noted, however, that there are degeneracies in mid-infrared eclipse observations between different potential atmosphere and surface compositions (Koll et al. 2019; Mansfield et al. 2019, 2024; Ih et al. 2023; Hammond et al. 2024) as well as between different thin atmosphere scenarios themselves (Ih et al. 2023; Lincowski et al. 2023; Zieba et al. 2023).

In this paper, we present a NIRISS/SOSS transmission spectrum of GJ 357 b, a super-Earth [$R_p = 1.217 \pm 0.084\,R_\oplus$, $T_{\rm eq} = 525 \pm 11$ K (assuming zero Bond albedo), $P = 3.93$ d and $M_p = 1.84 \pm 0.31 M_\oplus$] transiting a nearby M2.5V star (Jenkins et al. 2019; Luque et al. 2019). GJ 357 is a slow rotating mid-type M-star with a period of 78 ± 2 d (Luque et al. 2019), which was observed with HARPS to have an activity indicator $\log R'_{HK} = 5.53$ (Marvin et al. 2023) based on calcium line emission, making it one of the least active M-dwarfs in a survey of more than 4000 stars (Boro Saikia et al. 2018). For the rest of this work, we adopt the system parameters of Luque et al. (2019) as they are generally consistent with, but more precise than those of Jenkins et al. (2019) on account of including additional precise CARMENES and PFS RVs which were not considered in the latter study.

The layout of this paper is as follows: in Section 2, we present the description of our observations and outline our methodology for the data reduction and analysis. In Section 3, we present our analysis of the planet's transmission spectrum including atmospheric and internal modelling. In Section 4, we present modelling that constrains

the potential for GJ 357 b to have retained an atmosphere in the context of the evolution of the host star's ionizing luminosity. Then, in Section 5 we describe the potential for future observations of the planet, before concluding in Section 6.

2 OBSERVATIONS AND DATA ANALYSIS

We observed one transit of GJ 357 b with *JWST* using the Near Infrared Imager and Slitless Spectrograph (NIRISS) instrument (Doyon et al. 2023) in Single Object Slitless Spectroscopy (SOSS) mode (Albert et al. 2023). The observation began on the 2023 November 22 at 11:40:30 UT and finished at 17:10:32 UT. As the host star is relatively bright ($J = 7.3$), we used the SUBSTRIP96 subarray, which only includes the first SOSS diffraction order covering wavelengths 0.85–2.85 μm. The time series consists of 2201 total integrations with two groups per integration. This observation was part of the NIRISS Exploration of the Atmospheric diversity of Transiting exoplanets (NEAT) GTO programme (ID 1201 PI: Lafrenière).

2.1 Data reduction

We reduced the GJ 357 b time series observations using the `exoTEDRF` pipeline (Feinstein et al. 2023; Radica et al. 2023; Radica 2024), which has been widely employed to analyse both NIRISS (Coulombe et al. 2023; Lim et al. 2023; Cadieux et al. 2024; Fournier-Tondreau et al. 2024; Piaulet-Ghorayeb et al. 2024; Radica et al. 2024, 2025) and NIRSpec observations (Benneke et al. 2024, Schmidt et al. submitted; Ahrer et al. submitted).

We apply the standard `exoTEDRF` Stage 1 corrections (e.g. Radica et al. 2023, 2024; Piaulet-Ghorayeb et al. 2024) including superbias and non-linearity corrections, a time-domain cosmic-ray flagging routine (Radica et al. 2024), and ramp fitting. We additionally correct the $1/f$ noise at the group-level (i.e. before ramp fitting) using the `scale-achromatic` method (Radica et al. 2023; Radica 2024). In Stage 2, we perform the flat field correction and background subtraction using the STScI-provided SUBSTRIP96 background model. Notably, unlike in many other observations which employ the SUBSTRIP256 subarray (e.g. Lim et al. 2023; Cadieux et al. 2024; Fournier-Tondreau et al. 2024; Radica et al. 2024; Gressier et al. 2024b), we do not find that it is necessary to independently scale the background model before and after the background 'step' at column ∼750. As part of the Stage 2 calibrations, we also employ a principal component analysis (PCA) on the 2D detector images to reveal detector-level trends useful for light curve systematic detrending (e.g. Coulombe et al. 2023; Radica et al. 2025). As in most SOSS observations, our PCA reveals a sub-pixel drift in the trace position, as well as the characteristic beating pattern due to the telescope's thermal control (for more information see e.g. Coulombe et al. 2023). Finally, we extract the stellar spectra using a simple box extraction with an aperture width of 32 pix as the order self-contamination cannot be accurately modeled for SUBSTRIP96 observations (Radica et al. 2022a), and, in any case, is predicted to be negligible (Darveau-Bernier et al. 2022).

2.2 Light curve fits

We first summed all the stellar flux extracted from the detector to create a high-S/N white light curve. Unfortunately, as can be clearly seen in Fig. 1, our observations started roughly 10 min before the mid-transit point of GJ 357 b [propagating the mid-transit time from Oddo et al. (2023) to the date of our observations]. We tracked this down to discrepancies between the orbital ephemeris presented in Jenkins et al. (2019), which we used when constructing the *JWST* APT file for this observation as its quoted uncertainties were the lowest at the time, and the more accurate ephemeris from Luque et al. (2019). When propagated forward to the epoch of our observations, the transit times predicted from the Luque et al. (2019) or more recent Oddo et al. (2023) ephemerides agree with what we observed. However, using the Jenkins et al. (2019) ephemeris predicts a mid-transit time ∼1.5 h later. As a result, we only captured ∼60 per cent of the transit, and missed the entirety of ingress.

Nevertheless, we proceed to fit transit models to this light curve, using the flexible fitting package `juliet` (Espinoza, Kossakowski & Brahm 2019). Our light curve model consists of a `BATMAN` transit model (Kreidberg 2015), with six free parameters: the mid-transit time, T_0, the planet-to-star radius ratio, R_p/R_*, the scaled orbital semimajor axis, a/R_*, the planet's impact parameter, b, and the two parameters of the quadratic limb-darkening law following the Kipping (2013) parametrization. We additionally assume a circular orbit (Luque et al. 2019; Oddo et al. 2023).

We first test the light curve fit using wide, uninformative priors on all of the orbital parameters to see to what degree the transit shape can be accurately recovered from our observations – especially considering that ingress and egress in particular encode important information about the planet's orbital configuration and stellar limb darkening (Seager & Mallen-Ornelas 2003). With this method, we find what appears to be an adequate fit to the light curve, however, upon closer inspection, the orbital parameters are highly discrepant (often $> 3\sigma$) with the published values from Oddo et al. (2023). The mid-transit time, in particular, is off by $\sim 12\sigma$ compared to the time expected by propagating the Oddo et al. (2023) ephemeris (which is the most up-to-date). We then test putting a Gaussian prior on the mid-transit time, with a mean of the expected transit time (BJD = 2460271.0481) and width equal to the propagated uncertainty (0.000908 d) – based on the ephemeris from Oddo et al. (2023). In this case, we recover orbital parameters which are consistent with those of Oddo et al. (2023) and Luque et al. (2019) (i.e. $b = 0.213 \pm 0.118$, $a/R_* = 22.62 \pm 0.678$). We therefore, use this approach for our final fits.

There is correlated noise clearly visible in the post-transit baseline of our light curves, which is not modelled by the astrophysical model alone. To deal with this remaining noise, we include a systematics model that consists of a linear trend in time, as well as with the eigenvalue timeseries of the first two components identified by our PCA (i.e. the trace position drift and beating pattern). Including these in the systematics model decreases the residual point-to-point scatter by ∼20 per cent. Finally, we include an error inflation term added in quadrature to the existing flux errors. We use wide, uninformative priors for all components of the systematics model.

The best-fitting transit models are shown along with the white light curves in Fig. 1. Particularly visible in the third panel, there is correlated noise still present in the post-transit baseline which is not adequately captured by our systematics treatment described above. Gaussian processes (GPs) have been commonly employed to fit out unexplained systematics in NIRISS/SOSS light curves (e.g. Lim et al. 2023; Cadieux et al. 2024; Radica et al. 2024; Gressier et al. 2024b), particularly of smaller planets. Periodograms can potentially reveal periodicity in residual noise, potentially correlated with the stellar rotation period, which can then inform the choice of GP kernel (as is common in radial velocity analyses; e.g. Cloutier et al. 2017, 2019; Radica et al. 2022b). However, a periodogram of the baseline integrations does not reveal any significant power at a specific periodicity.

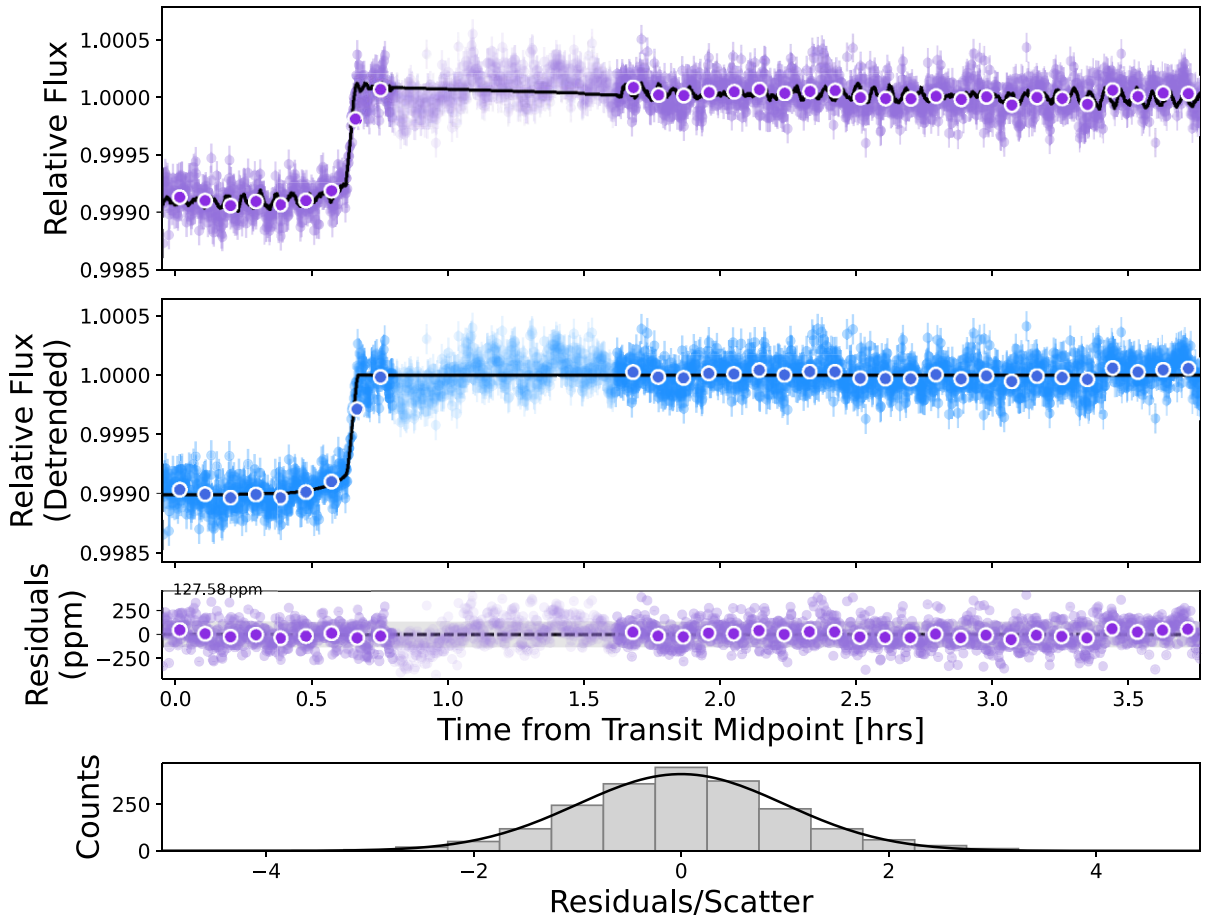

Figure 1. GJ 357 b NIRISS white light curve fit results. *Top panel*: raw GJ 357 b order 1 white light curve, with the best-fitting astrophysical transit + systematics model overplotted in black. The first ∼40 per cent of the transit was missed by our observation. Integrations from ∼0.8 to1.5 h post-transit mid-point (shown as faded) were excluded from the fit due to uncorrectable systematics. *Second panel*: systematics corrected white light curve, with the best-fitting astrophysical model overplotted in black. *Third panel*: residuals to the light curve fit. Some correlated noise remains in the post-transit baseline which is not adequately captured by our systematics model. *Bottom panel*: histogram of residuals.

We also tried employing a GP with a critically damped simple harmonic oscillator (SHO) kernel via the `celerite` package (Foreman-Mackey et al. 2017), which has proven effective at modelling stellar granulation noise in both *Kepler* (Kallinger et al. 2014; Foreman-Mackey et al. 2017; Pereira et al. 2019) and *JWST* (Radica et al. 2024; Coulombe et al. 2025) light curves. Though, since there is no pre-transit baseline to anchor the GP model, its behaviour is essentially unconstrained during the transit itself, which resulted in clearly unphysical light curve models. This same behaviour persisted irrespective of the axis on which the GP was trained (e.g. time, detector PCs, etc.), the prior restrictions we placed on the GP timescale, as well as the chosen GP kernel itself. We therefore elect not to include any GPs in the final light curve model.

Finally, we note that the worst offending region for residual correlated noise in the baseline seems to be the region from ∼0.8 to 1.5 h post-mid-transit. We thus try repeating our fits without any GP models, but cutting these particular integrations. This test does not result in any significant change to either the inferred orbital parameters, or the final transmission spectrum (e.g. Fig. B1), indicating that the residual correlated noise does not have a substantial impact on the transmission spectrum. However, in order to be as conservative as possible, we elect to use the transmission spectrum from the fits where these integrations are cut in the remainder of our analysis.

In order to produce the transmission spectrum itself, we first bin the light curves to a constant resolution of $R = 50$. This resolution provides an adequate trade-off between having sufficient S/N in individual wavelength bins to accurately model correlated noise, while still well-sampling potential atmospheric features that we hope to detect via Gaussian feature or forward model analyses (e.g. Alam et al. 2024; Alderson et al. 2024, 2025; Scarsdale et al. 2024). We then fit the same astrophysical + systematics model described above, but we fix the orbital parameters to the best-fitting values from the white light curve fit. Additionally, as coverage of ingress and egress are critical for constraining limb-darkening parameters, freely fitting the limb-darkening results in broadly unconstrained posteriors and imprecise transit depths. We, thus, put a Gaussian prior on the quadratic limb-darkening terms for each bin, with the mean value set to the prediction from the EXOTIC-LD package (Grant & Wakeford 2024) using the 3D Stagger grid (Magic et al. 2015), and widths of 0.2 (Patel & Espinoza 2022). The fitted limb-darkening values are shown in Fig. B2. Our final spectroscopic fits therefore have eight free parameters: the transit depth and limb darkening, as well as the five parameters of the systematics model describing the transit zero

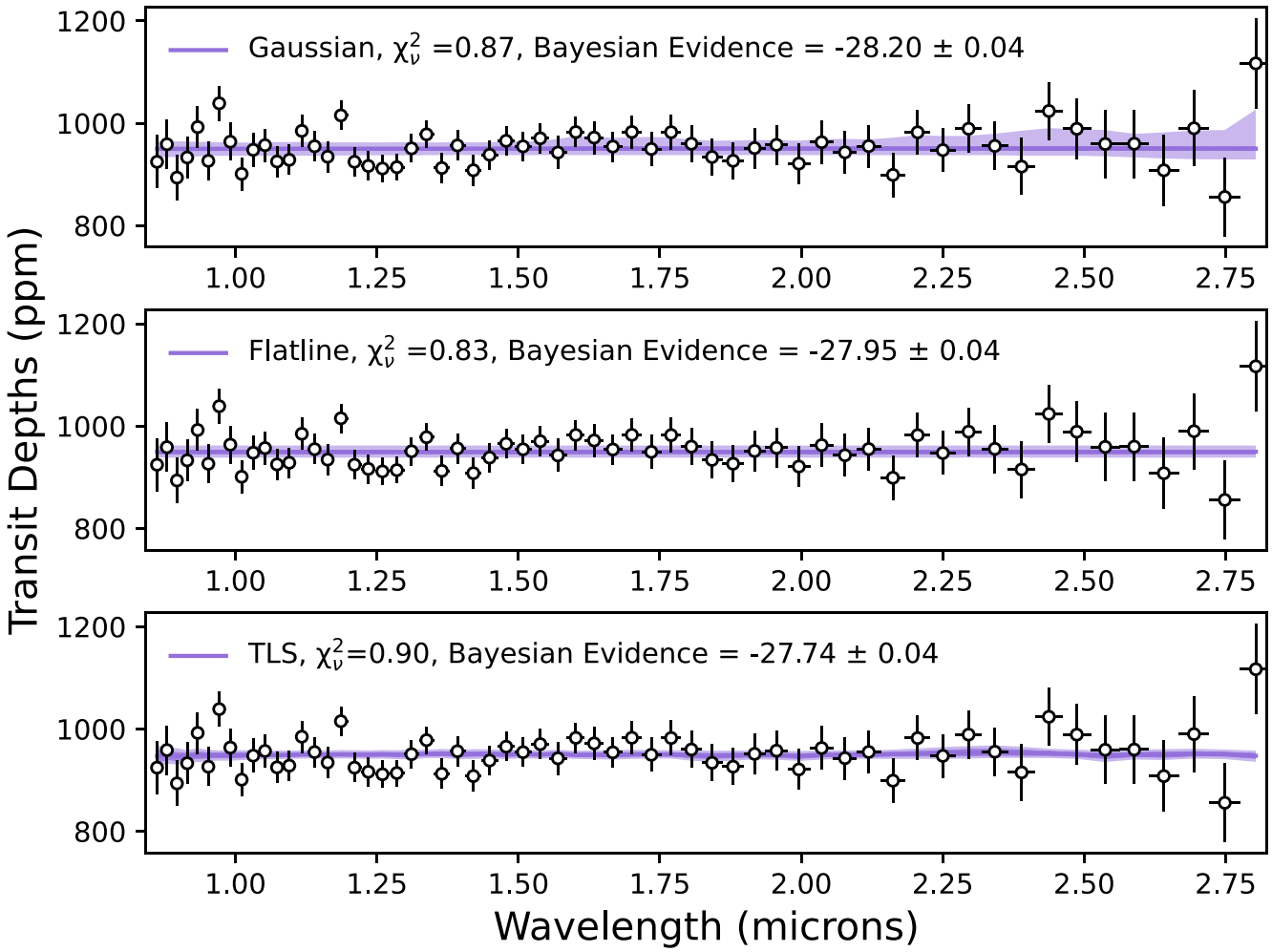

Figure 2. *Top panel*: best-fitting Gaussian model. *Middle panel*: flat line model. *Bottom panel*: best-fitting TLS model. We present the median, 1σ, and 3σ contours in purple for the Gaussian model and 1σ, and 2σ contours for the flat line and TLS models. It can be seen there is some non-flat structure detected within the 3σ contour of the Gaussian model, however, this model is not favoured over the flat line or TLS model.

point, linear trends with time and the first two PCA eigenvalue time series, and the error inflation term. The final transmission spectrum is shown in Figs 2 and 3.

We note that despite the above challenges, we still obtain a transmission spectrum that is sufficiently precise to assess the presence of potential atmosphere scenarios on GJ 357 b. Particularly in the context of 'previous generation' observations of small planets with the *Hubble Space Telescope* where important science was still accomplished despite routinely achieving transit depth precisions >100 ppm at ∼1.4 μm (Wit et al. 2016; Wakeford et al. 2019; Garcia et al. 2022). For comparison, we reach a precision of ∼40 ppm at these wavelengths. None the less, in Fig. B1, we compare our achieved transit depth precision to what we could have obtained if we had observed the full transit (and assuming the same level of light curve scatter) as well as the photon noise precision. We find that our transmission spectrum is ∼25 per cent less precise than if the full transit was captured and ∼34 per cent less than the photon noise precision. The transit depth precisions that we reach, therefore, compare well with previous studies aiming to quantify the compositions of rocky planet atmospheres (e.g. Alam et al. 2024; Alderson et al. 2024, 2025; Scarsdale et al. 2024).

3 TRANSMISSION SPECTRUM AND RESULTS

To assess the physical contents of the spectrum we perform three sets of tests: a Gaussian feature detection analysis, a stellar contamination (via the TLS effect) exploration, and a comparison with a grid of forward models. We opt to not perform a full Bayesian spectral retrieval which is common to interpret the atmospheres of terrestrial planets (e.g. Lim et al. 2023; Radica et al. 2025). Given the partial transit and lack of identifiable spectral features, we believe this level of analysis is not warranted for these observations.

3.1 Feature detection

We initially explore whether the data support any deviations from a flat line, namely any Gaussian features, which could be analogous, and roughly approximate, the broad-band features of H_2O, CH_4 or CO_2 (e.g. JWST Transiting Exoplanet Community Early Release Science Team 2023; May et al. 2023; Moran et al. 2023; Scarsdale et al. 2024).

Following the previous work, we parametrize a spectral feature, while remaining agnostic to the particular gas causing the feature,

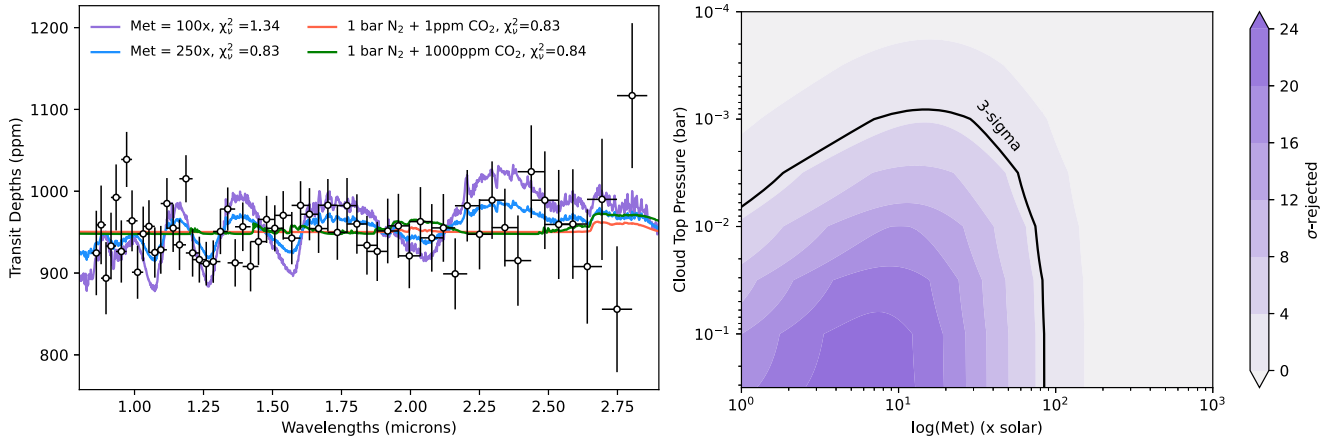

Figure 3. *Left*: transmission spectrum of GJ 357 b with four atmospheric models overplotted. The reduced χ^2 for each model is quoted in the legend. We show two models from our grid analysis: 100× and 250× solar metallicity. Each model has an opaque cloud layer at 0.1 bar, we assume this to be analogous to the tropopause of Solar system objects (Robinson & Catling 2014). We also show two nitrogen rich models that would be distinguishable with MIRI, as explained in Section 5. *Right*: contour plot showing the σ-rejection of atmospheric models as a function of cloud top pressure and metallicity. The 3σ contour is denoted with the solid black line.

with a Gaussian function:

$$f(\lambda, A, \mu, \sigma_m, b) = A \exp\left(-\frac{(\lambda-\mu)^2)}{2\sigma_m^2}\right) + b, \quad (1)$$

where μ, σ_m, and A are the centre, standard deviation, and amplitude of the Gaussian, respectively. The parameter b is a vertical offset. We fit this model to our data and present the results in Fig. 2 along with the results for a flat line fit – i.e. using a model of the form:

$$f(\lambda, b) = b. \quad (2)$$

We set our priors for the amplitude of the Gaussian to be [−2,3] in log-space in units ppm, the centre of the Gaussian [0.6,3.0] in uniform space and units of microns, the standard deviation of the Gaussian to be [−2,0.3][1] in log-space with unit microns, and the offset vertical position of the spectrum baseline to be [800,1200] in units ppm. The same priors for the offset are used for our flat-line model. We use the nested sampling algorithm PYMULTINEST (Buchner et al. 2014) with 2000 live points and an evidence tolerance of 0.5.[2] We then compare the Bayesian evidence produced from the Gaussian model and flat line model to determine if any features are detected within the data.

We present the best-fitting range of Gaussian models in Fig. 2. We find a Bayesian evidence (ln(Z)) of −28.20±0.04 compared to −27.95±0.04 for the flat line model. We compare these values using the methodology of Trotta (2008), whereby the Bayes factor = ln(Z_1) − ln(Z_2). In our case, Z_2 is our flat line model. The larger number indicates that model is supported more by the data. Thus, we find that the Bayes factor is smaller than 1, and therefore there is inconclusive evidence for any features. In fact, given the slightly larger Bayesian evidence from the flat line model, the data slightly support the flat line.

Next, we conducted an array of more physically motivated feature searches, by fixing the position of the Gaussian bump to the wavelengths of known water and methane band heads. Namely for water: 0.95, 1.15, 1.4, and 1.85 μm, and for methane: 1.7 and 2.3 μm. For water, we find the following Bayesian evidences: 0.95 μm (−28.35± 0.04), 1.15 μm (−28.44± 0.04), 1.4 μm (−28.39± 0.04), and 1.85 μm (−28.32± 0.04). For methane, we find the following Bayesian evidences: 1.7 μm (−28.11± 0.04) and 2.3 μm (−28.23± 0.04). All of these models are less favoured compared to the flat line model. Lastly, we perform the same test at 2.8 μm, as this corresponds to a CO_2 band, we find a Bayesian evidence of −28.03 ± 0.04. Therefore, even with our informed prior, we still conclude there to be no features detected within the data. These tests have become important to conduct for observations with low signal-to-noise (Taylor 2025).

3.2 Transit light source effect modelling

As stated in Section 1.1, previous observations have concluded that GJ 357 is an inactive star, thus we should not see any impacts on the resultant transmission spectrum from the star. We test this by performing a suite of TLS fits to our observations. We model the TLS in a similar fashion to the implementation in POSEIDON (MacDonald 2023), assuming four different set-ups for the star:

(i) A three-parameter model that assumes a photosphere temperature ($T_{\rm phot}$), a heterogeneous region temperature ($T_{\rm het}$), and the photosphere covering fraction of the heterogeneity ($f_{\rm het}$).
(ii) The same as above however with log(g) as free parameter.
(iii) A five-parameter model that fits for the photosphere temperature ($T_{\rm phot}$), spot temperature ($T_{\rm spot}$), spot fraction ($f_{\rm spot}$), faculae temperature ($T_{\rm fac}$), and faculae fraction ($f_{\rm fac}$).
(iv) The same as above but with two additional parameters, the log(g) for the spot and faculae regions.

We model the stellar spectra using the PHOENIX grid of models (Husser et al. 2013), interpolating using the python package PYSYNPHOT (STScI Development Team 2013). We model the atmosphere assuming it is a flat line. We find the Bayesian evidences to be −28.19 ± 0.04, −28.48 ± 0.03, −27.74 ± 0.04, and −28.92 ± 0.04, for models (i), (ii), (iii), and (iv), respectively. They all provide similar fits to the data, with model (iii) providing the best fit, and only slightly favoured compared to the flat line model. The Bayes factor between the TLS model and flat line is less than 1, and therefore there is no conclusive evidence for this more complex model. We

[1]The prior choice was made as the lower limit is not smaller than our bin-width, and the upper limit is larger than the feature shape, if present.
[2]The evidence tolerance and sampling efficiency are the defaults for PYMULTINEST and recommended for use by the developer.

can, therefore, conclude that the impact of stellar contamination is minimal. We have plotted the best-fitting models from model (iii) in the bottom panel of Fig. 2.

3.3 Comparison with atmospheric forward models

Although both previous analyses do not provide strong evidence for the presence of an atmosphere, flat spectra can also be a result of high atmospheric mean molecular weights or high-altitude clouds. In order to assess what we can physically say about a potential atmosphere on GJ 357 b, we use `CHIMERA` (Line et al. 2013) which has recently been coupled with `FastChem2` (Stock, Kitzmann & Patzer 2022; see Schlawin et al. 2024, for implementation) to generate a grid of atmosphere models as a function of metallicity and cloud top pressure. Similar to Alderson et al. (2024), we generate our grid from 1 to 1000× solar metallicity, log-spaced with 26 grid points, and cloud top pressure from 10 to 10^{-4} bar, log-spaced with five grid points. For the pressure–temperature profile, we opt for an isothermal temperature fixed at the equilibrium temperature of 525 K, and we assume that the elemental C/O ratio is solar (where the solar value is 0.55; Asplund et al. 2009). We include the following opacities in our model: H_2O (Freedman et al. 2014; Polyansky et al. 2018), CO_2 (Freedman et al. 2014), CO (Rothman et al. 2010), CH_4 (Rothman et al. 2010), HCN (Barber et al. 2014), and NH_3 (Coles, Yurchenko & Tennyson 2019). We also model the H_2–H_2 and H_2–He collision-induced absorption (CIA) (Richard et al. 2012). We restrict the opacity sources to these as they have prominent absorption cross-sections across the NIRISS/SOSS spectral range (Feinstein et al. 2023; Taylor et al. 2023). With our grid, we perform a χ^2 analysis by fitting each model to the transmission spectrum, computing the rejection sigma as a result.

To compute the confidence to reject the model, we use the following equation:[3]

$$\sigma = \frac{\chi^2 - \mathrm{DOF}}{\sqrt{2 \times \mathrm{DOF}}}, \tag{3}$$

where DOF is the degrees of freedom.

We perform this fitting using PYMULTINEST with one free parameter, the offset between the forward model and the data. We adopt a wide uniform prior for this parameter, as the offsets between the forward model and the data can be large. We show a subset of the models in the left panel of Fig. 3 and a contour plot displaying the rejection sigma as a function of cloud top pressure and metallicity in the right panel. We plot a black line to highlight the 3σ level. Essentially, we can rule out atmospheres that have cloud top pressures higher than around 0.01 bar and metallicities up to around 100× solar.

In the left panel of Fig. 3, we plot a subset of atmospheric models with an associated reduced χ^2. We plot the nitrogen rich atmospheres described in Section 5, alongside models with metallicity of 100× and 250× solar. We also consider pure 'end-member' atmospheres, specifically pure H_2O, CO_2, and CH_4 and show these in Fig. B3. In each of these models, we assume a nominal cloud top pressure of 0.1 bar, which is typically where the tropopause is in Solar system objects (Robinson & Catling 2014). For all cases apart from 100× solar metallicity, the models provide similar fits to the data, with a reduced χ^2 of less than 1 indicating that we are overfitting, thus we cannot distinguish between these models. Given that we have 60 data points, we would expect a χ^2 distribution with 59 degrees of freedom and a variance of 118. As we have a sufficiently large number of degrees of freedom, the χ^2 distribution can be approximated as a Gaussian distribution, therefore, we expect the reduced χ^2 for our best-fitting model to be drawn from a Gaussian distribution with a mean of unity and a standard deviation of 0.092. Where the standard deviation is taken to be 1 over the root of the variance. The 100× solar metallicity model, with a reduced χ^2 of 1.34, can be confidently rejected – as seen from our rejection tests in the right panel of Fig. 3. We also explore the dependence of the C/O ratio and find that this parameter is unconstrained for this quality of data (see Appendix A).

[3]Taken from section 7.2.1 in Gregory (2005).

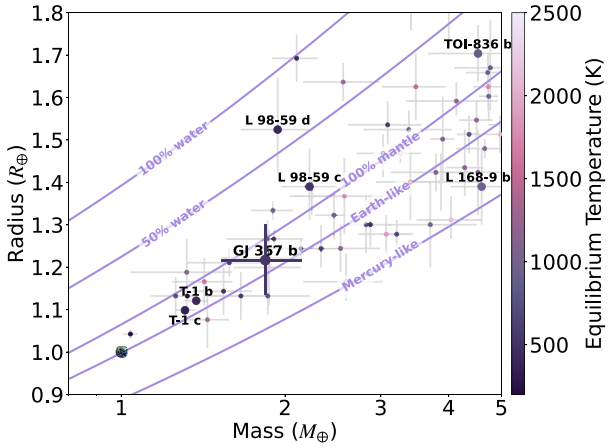

Figure 4. Mass–radius diagram for selected rocky exoplanets retrieved from the DACE data base, with planets colour-coded by their equilibrium temperature. The solid curves represent composition models assuming three-layered planetary interiors: a metallic core, a silicate mantle, and a water layer. Planets with published transmission spectra are highlighted in bold. T-1 b and c corresponds to TRAPPIST-1 b and c. GJ 357 b is highlighted as consistent with an Earth-like composition.

3.4 Interior and bulk composition modelling

Fig. 4 shows the mass–radius diagram for potentially rocky exoplanets retrieved from the Data & Analysis Center for Exoplanets (DACE) data base. Each planet is colour-coded by its equilibrium temperature. The figure also shows several hypothetical composition curves, which we modelled using the open-source interior structure code MAGRATHEA (Huang, Rice & Steffen 2022). MAGRATHEA solves the hydrostatic equilibrium equations to determine planetary radii for a given mass, based on specified bulk compositions divided into three distinct layers: a metallic core, a silicate mantle, and a water layer. The Earth-like composition assumes 32.5 per cent Fe and 67.5 per cent silicates (upper mantle consisting of forsterite, wadsleyite, and ringwoodite and lower mantle consisting of bridgmanite and post-perovskite), representing a metallic core and silicate mantle structure similar to Earth. The 100 per cent-mantle line corresponds to a planet consisting entirely of $MgSiO_3$, with no core. The Mercury-like curve corresponds to a planet dominated by a metallic core (67 per cent Fe, 33 per cent $MgSiO_3$). The 100 per cent-water line indicates a planet composed entirely of water (in liquid and high-pressure ice form with a surface temperature of 300 K), while the 50 per cent-water line represents a planet with 50 per cent water layer over an Earth-like mantle and core (16.25 per cent Fe and 33.75 per cent $MgSiO_3$).

The mass–radius diagram shows that the bulk composition of GJ 357 b is consistent with an Earth-like interior. However, determining the interior structure of a planet based solely on its mass and radius (i.e. its bulk density) is a highly degenerate problem (e.g. Rogers &

Seager 2010; Unterborn et al. 2022; Guimond et al. 2024; Haldemann et al. 2024). If considering a three-layered planet, at least one of the three layers (core, mantle, hydrosphere) must be fixed to constrain the ratio of the other two layers. Additionally, uncertainties in the composition of each layer, such as the amount of lighter elements in the core (e.g. Hirose, Wood & Vočadlo 2021) or iron content in the mantle (e.g. Unterborn, Dismukes & Panero 2015; Hakim et al. 2018), further complicate determining the relative proportions of each layer. While GJ 357 b's bulk composition aligns with an Earth-like interior, it is equally consistent with alternative configurations, such as a higher core-to-mantle fraction including a hydrosphere or a H/He envelope (or both). For instance, GJ 357 b's mass and radius are equally consistent with a hypothetical interior structure consisting of a pure iron core (with no silicate mantle) and a water layer of approximately 0.54 Earth masses. Similarly, the planet's interior bulk composition could be reproduced with an Earth-like silicate mantle and core (core-mass-fraction of 0.325) and a H/He layer of roughly 0.045 Earth radii. Measuring the host star's Mg/Si and Fe/Si elemental ratios has been proposed to help lift this degeneracy (Sotin, Grasset & Mocquet 2007; Dorn et al. 2017a; Dorn, Hinkel & Venturini 2017b; Spaargaren et al. 2023).

4 THE POTENTIAL FOR AN ATMOSPHERE

Efforts to detect rocky exoplanet atmospheres with the *JWST* are hindered by several factors, including the intense irradiation environments of M-dwarf host stars, which can remove the atmospheres of highly volatile-rich planets (Ji et al. 2025), degeneracies inherent in secondary eclipse observations (Hammond et al. 2024), and stellar contamination in transmission spectra (Radica et al. 2025). This section discusses why, despite the non-detection of an atmosphere in our observations of GJ 357 b, its highly inactive M-dwarf host star makes it a relatively strong candidate for follow-up observations aimed at detecting a retained high-MMW atmosphere.

The flat transmission spectrum presented here is consistent with the theoretical expectation of escape of a primordial hydrogen atmosphere from GJ 357 b. Absorption of X-ray (1 − 10 nm) and extreme ultraviolet (EUV) (10 − 91 nm) irradiation, altogether XUV, releases photoelectrons that effectively heat the thermosphere and can drive transonic escape, similar to the solar wind predicted by Parker (1958). The low mass of the host star (0.34 $M_\odot$) means GJ 357 b sees a long and intense saturated phase of ionizing radiation, contributing to a large enough lifetime XUV fluence to, in principle, remove a volatile inventory greater than the present-day mass of the planet (e.g. Watson, Donahue & Ker 1981; Modirrousta-Galian et al. 2020). As such, GJ 357 b is placed on the airless side of the (XUV) cosmic shoreline (Zahnle & Catling 2017). However, a high-molecular-weight atmosphere is more resilient to photovaporation and could be outgassed later in the star's evolution – its presence would also be consistent with our featureless spectrum.

The escape of atmospheres dominated by metals (e.g. C, N, and O) rather than hydrogen is not well explored. Simulations of escape of an Earth-like atmosphere by Nakayama et al. (2022) found that atomic line cooling prevented rapid loss for extreme fluxes of ionizing radiation, up to at least 4 W m^{-2}, perhaps precluding bulk escape altogether. However, Chatterjee & Pierrehumbert (2024) calculated that a highly ionized Earth-like thermosphere is unstable to escape at lower temperatures ($\lesssim$ 4500 K) compared to those assumed by Nakayama et al. (2022) due to the electrons dragging out ions to space via an ambipolar electrostatic field, effectively reducing mean molecular weight. Chatterjee & Pierrehumbert (2024) suggest that at high XUV fluxes the escape of a secondary atmosphere from a super-Earth, such as GJ 357 b, would take the novel form of a global ion outflow of metals, limited by a thermostat mechanism between photoionization heating and atomic line cooling.

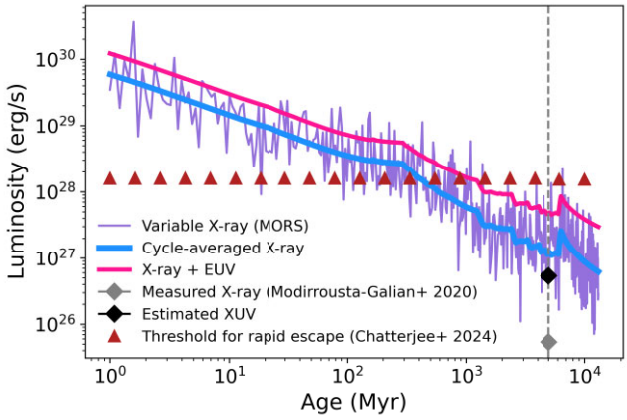

Figure 5. Models of the evolution of the luminosity of GJ 357 in the X-ray and EUV bands. The *XMM–Newton measurement* of the X-luminosity (grey diamond) with the estimated age of 5 Gyrs are taken from Modirrousta-Galian et al. (2020). The XUV luminosity (black diamond) is estimated from the *XMM–Newton* measurement using scaling relationships from Johnstone et al. (2021). In blue, is the cycle-averaged lowest-activity X-ray track in the evolution of a model cluster of stars of mass 0.34$M_\odot$ in MORS (Johnstone et al. 2021). The threshold in the XUV luminosity for GJ 357 to drive the hypothetical transonic outflow of a secondary atmosphere on planet b is roughly $10^{28.2}$ erg s^{-1}. The MORS XUV luminosity (in pink) drops below the threshold for rapid escape (Chatterjee & Pierrehumbert 2024) at approximately 10^3 Myr.

4.1 Evolution of ionizing luminosity

To estimate the evolution of the photoevaporation regime of GJ 357 b we use MORS (Johnstone et al. 2021), a physical rotational evolution model of the high energy emission of stars that is constrained by observed rotational and X-ray distributions in stellar clusters. Direct measurements of the X-ray luminosity are also available with *XMM–Newton* from Modirrousta-Galian et al. (2020), which found $\log L_x \left[\text{ergs}^{-1}\right] = 25.73 \pm 0.23$ (grey diamond, Fig. 5). At such a relatively small X-ray surface flux, the EUV emission is relatively enhanced: we calculate with scaling relations from Johnstone et al. (2021) that the corresponding total XUV luminosity is an order of magnitude higher (black diamond, Fig. 5). Fig. 5 shows that the measured X-ray luminosity is more than an order of magnitude below the main-sequence cycle-average for a star of mass 0.34$M_\odot$ following the lowest activity track available from MORS (blue, Fig. 5; Johnstone et al. 2021). The purple track on Fig. 5 shows the estimated intrinsic variability: the X-ray luminosity will exceed the long-term average by a factor of 3 roughly 10 per cent of the evolution phase (Johnstone et al. 2021). Even the troughs of the (lowest activity tracks) variable X-ray evolution are significantly higher than the measured luminosity, showing that GJ 357 b is exceptionally inactive. However, though unlikely for a random sample, it is possible that GJ 357 was observed in an unusually quiescent period and that the long-term average is somewhat higher.

Modirrousta-Galian et al. (2020) estimated a minimum age of 5 Gyr for GJ 357 based on the lower bound X-ray activity track for a homogeneous grouping of M-dwarfs from Penz & Micela (2008), but this method of estimation does not account for GJ 357 being a mid-M star (M2.5V). We can estimate the age of GJ 357 based on when

the rotation period from MORS evolves to that observed of roughly 80 d, which yields roughly 2.3 Gyr. However, given the MORS discrepancy with the measured X-ray luminosity, this estimate is also flawed. Finally, we can compare the observed $\log R'_{HK} = 5.53$ activity proxy (Marvin et al. 2023) to trends in an up-to-date M-dwarf sample from Engle (2023) to estimate a mean minimum age of 4 Gyr.

Applying the model from Chatterjee & Pierrehumbert (2024) to an upper atmosphere on GJ 357 b dominated by carbon and oxygen, we find the threshold in ionizing radiation to drive transonic escape is $\sim 10^3 F_{\mathrm{xuv},\oplus}$ with a rate of roughly a bar per 2 Myr, where the present XUV flux at Earth is given by $F_{\mathrm{xuv},\oplus} \approx 4 \times 10^{-3}$ Wm^{-2}. Note that if we instead took the lower bound on the mass of GJ 357 b of 1.53M$_\oplus$, the threshold would be reduced by less than a factor of 2, which is not enough to change the conclusions made here. Overall, the threshold estimate represents a middle ground between an extrapolation of Nakayama et al. (2022), which suggests rapid escape would not occur, and the range of atmospheric heating and dynamics that could enhance escape efficiency (e.g. Cohen et al. 2024). Thus, we argue that the possibility of build-up of a secondary atmosphere is limited to when GJ 357 b is old enough that ionizing radiation fluxes have decayed significantly below the best estimate for the threshold for transonic escape (see Fig. 5).

The cycle-averaged XUV luminosity from MORS does not meet the model threshold for bulk escape after 1 billion years (Fig. 5). On taking into account the XUV variability, the MORS track would meet the threshold periodically afterwards. Thus, based on the *model* low-activity track for a star with the same mass as GJ 357 b, an accumulation of tens of millions of years meeting the threshold could lead to tens of bars of outgassed CO_2 being lost, making revival of a secondary atmosphere difficult. However, the *measured* exceptionally low activity means that the cycle-averaged XUV luminosity should have becomes sub-threshold earlier and the steeper time-decay required should severely limit the ability of variability to contribute rapid escape over billions of years. So GJ 357 is significantly more conducive to a retained secondary atmosphere compared to other M2.5V stars.

4.2 Possible evolution to a retained atmosphere

In the saturated phase, the loss of a massive primordial hydrogen envelope could strip a planet down to a bare rock. At this stage, volatile escape becomes limited by the rate of outgassing until XUV irradiation decreases below the threshold for rapid photoevaporation. Once this occurs, an atmosphere can gradually accumulate through volcanic activity. Noting that the MORS track significantly overestimates the present X-ray luminosity (Fig. 5), we estimate that from 500 to 2000 Myr, a growing secondary atmosphere would likely only leak mass to space rather than escape as a hydrodynamic wind.

The pre-dominant leak of atmospheric mass is likely to be from stellar wind erosion. To estimate this effect, we compare GJ 357 to the similar-sized but significantly more active star GJ 414 (0.39M$_\odot$), for which an upper bound on stellar mass loss is constrained to be less than 10 per cent of the Sun's rate (Wood et al. 2021). This upper bound aligns closely with the best estimate for the mass loss rate of TRAPPIST-1 (Dong et al. 2018). Accordingly, we infer the atmospheric escape rate by scaling from magnetohydrodynamic simulations of TRAPPIST-1 b's erosion at 1 bar Myr^{-1} (Canto & Raga 1991; Dong et al. 2018), adjusting for the $\sim 1/9$ lower wind flux at the $\sim 3\times$ greater semimajor axis of GJ 357 b. Finally, given that stellar wind strength is reduced around less active stars (Wood et al. 2021), we estimate that, GJ 357 b's atmospheric erosion rate would remain well below 0.1 bar Myr^{-1} once on the main sequence.

For a 1.84M$_\oplus$ stagnant-lid planet Dorn et al. (2018) find outgassing rates of ~ 10 bar Gyr^{-1} for an initial Earth-like mass concentration of radiogenic elements but with considerable sensitivity to various mantle properties. This is similar to the volcanism rate of Earth's mid-ocean ridges, which was adopted by Kite & Barnett (2020) with scaling proportional to mantle depletion. Even though there is significant uncertainty, that the best guess for supply exceeds loss by 2 orders of magnitude provides some confidence that revival is a distinct possibility. Thus, from the perspective of star–planet interaction and evolution, it is possible that an atmosphere of several to several tens of bars is retained today.

4.3 Limitations

Along with the dynamics of rapid escape of secondary atmospheres being relatively unexplored (Chatterjee & Pierrehumbert 2024), there are two major unknowns in this analysis. First, our modelling cannot rule out airlessness due to the possibility that GJ 357 is frequently in a highly energetic flare state (e.g. France et al. 2020; Diamond-Lowe et al. 2024). Though flares represent less of a problem for GJ 357 b than the overall M-dwarf rocky planet population due to the sub-threshold characteristics already discussed. Second, a mantle depleted during the early phase of volatile loss could, in principle, entail later outgassing reduced to $\lesssim 0.1$ bar Gyr^{-1}. Krissansen-Totton et al. (2024) modelled how a long-lived magma ocean on TRAPPIST-1 b enabled catastrophic depletion of the mantle via photoevaporation. However, we note that present-day XUV irradiation of GJ 357 b is 2 orders of magnitude lower than at TRAPPIST-1 b and it would have seen a much shorter and less intense saturated phase, so an extrapolation to similar depletion would be pessimistic.

5 PREDICTIONS FOR FUTURE CHARACTERIZATION

One key endeavour of the exoplanet community is to detect atmospheres around terrestrial planets, and subsequently, measure their composition. GJ 357 b is a prime candidate to have retained an atmosphere, as discussed in Section 4, therefore, we compute the feasibility of detecting an atmosphere using MIRI. Our analysis is partially motivated by the 500-h Rocky Worlds DDT programme (Redfield et al. 2024), which plans to observe this planet as it is well suited to emission spectroscopy.

We model the mid-infrared emission spectra of a small selection of possible atmospheres and surfaces to determine the possibility of measuring their spectral features. We follow the methodology described in Hammond et al. (2024), using the *AGNI* model to simulate 1D atmospheres and surfaces with variable albedo and emissivity. From the larger sample modelled in Hammond et al. (2024), we chose to model bare-rock surfaces with low and high albedos (tholeiitic basalt and lunar anorthosite), and 1 bar N_2 atmospheres with 1 ppm and 1000 ppm of CO_2. These highlight the detectable effects of non-zero albedo, surface spectral features, greenhouse warming of the surface, and the large CO_2 absorption feature at 15 μm. We model the observed emission spectra using `PandExo` (Batalha et al. 2017) for MIRI/LRS, and using the instrumental throughputs for the MIRI filters (Luger, Lustig-Yaeger & Agol 2017).

Fig. 6 shows the resulting emission spectra, for MIRI/LRS (circles) and for the MIRI *F*1130*W*, *F*1280*W*, *F*1500*W*, and *F*1800*W* photometric filters (squares). It shows how variations in the emission spectra will be detectable with just two eclipses, but that strong degeneracies exist between different types of atmosphere and surface, as discussed in Hammond et al. (2024). For example, an atmosphere

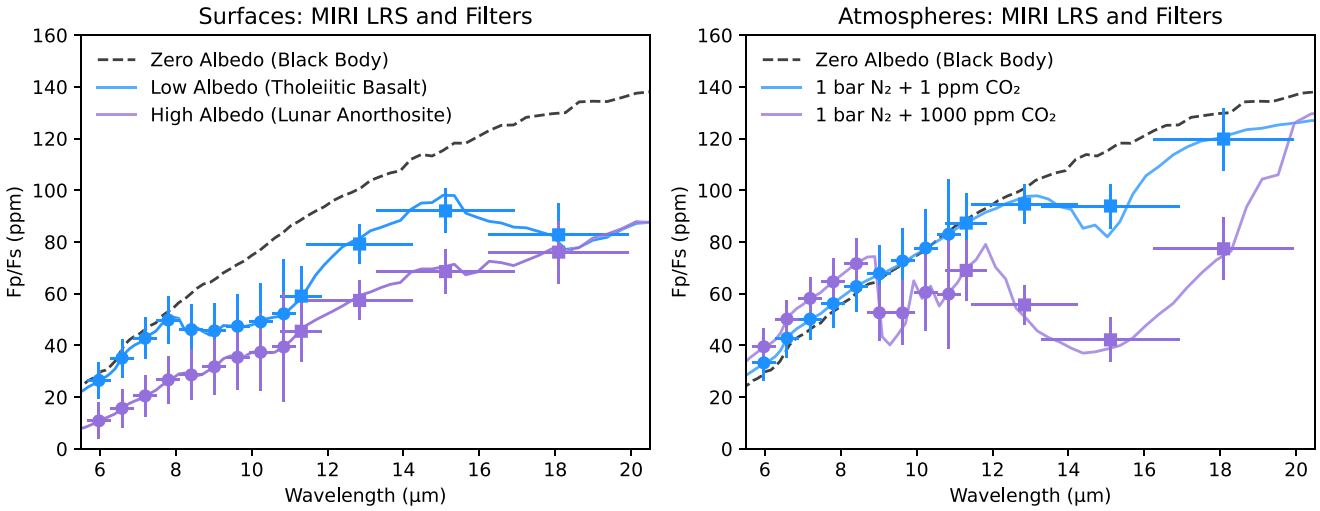

Figure 6. Modelled MIRI LRS and photometric filter emission spectra for GJ 357 b, for simulated surfaces and atmospheres following the methodology of Hammond et al. (2024). *Left panel*: two bare-rock surfaces, with modelled MIRI/LRS (circles) and MIRI filter (squares) emission for two observed eclipses. *Right panel*: two 1-bar atmospheres, with modelled MIRI/LRS and MIRI filter emission for two observed eclipses. The limited set of cases here are distinguishable from each other at this level of precision given enough spectral coverage, but strong degeneracies exist between observations of individual photometric points.

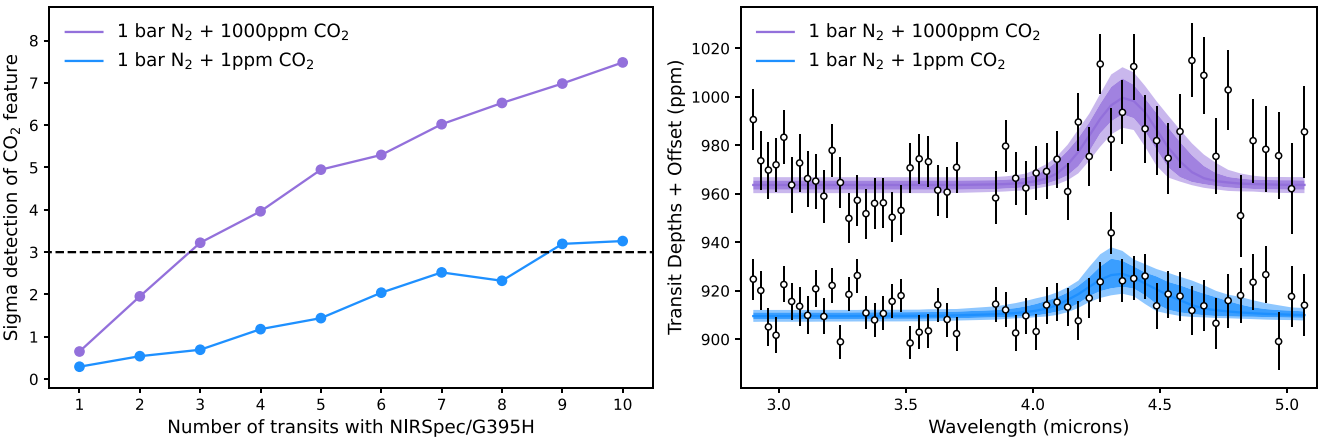

Figure 7. The ability to detect a N_2-dominated atmosphere with varying levels of CO_2 using NIRSpec/G395H. *Left*: we present the detection significance, based on fitting a Gaussian to the 4.3 μm CO_2 feature, as a function of the number of stacked transits. In purple, we show the results from 1 bar N_2 atmosphere with 1000 ppm CO_2, and in blue, we show the results from 1 bar N_2 atmosphere with 1 ppm CO_2. The horizontal black line represents the 3σ threshold, above which can be considered a detection. *Right*: we plot the best-fitting models for the lowest number of transits that provides a greater than 3σ detection of the CO_2. We add a 50 ppm offset between the two cases to help visibility.

with sufficient CO_2 could produce notably lower emission particularly around 10 μm or 15 μm, which might be distinguishable from the lower levels of spectroscopic variation for surfaces in general (Hu, Ehlmann & Seager 2012). This could be detected with observations in multiple filters or with MIRI LRS (Zieba et al. 2023). Heat redistribution could also lower the total emission from the day-side of an atmosphere by a detectable amount (Seager & Deming 2009; Koll et al. 2019), although this may be degenerate with the cooling effect of a high-albedo bare-rock surface (Hammond et al. 2024). Further observations of transmission spectra may be necessary to break this degeneracy, as phase curve observations may be too time-consuming for this planet given its 3.93-d orbital period.

We explore how many transits would be required to detect the 4.3 micron CO_2 feature for both the atmospheres modelled in Fig. 6. We take the nitrogen-rich transmission spectra plotted in Fig. 3 and use `PandExo` (Batalha et al. 2017) to simulate NIRSpec/G395H observations for a resolution of 50. We inject Gaussian noise to the data, centred on the mean value at each wavelength with a standard deviation based on the size of each observational error calculated at each wavelength. We perform our Gaussian feature analysis to determine whether the CO_2 feature can be detected and to what sigma can we detect it compared to a flat line model. We do this as a function of transits, assuming that the error on the observations scale as a function of $1/\sqrt{N}$, where N is the number of transits. However, we note that NIRSpec/G395H observations have been shown not to bin down as $1/\sqrt{N}$ (e.g. Alderson et al. 2024), so our tests should be treated as an optimistic scenario. For each number of transits, we consider 100 different noise realizations, which we average over to obtain the final detection threshold shown in Fig. 7. We find for a 1 bar N_2 atmosphere with 1000 ppm of CO_2, we can detect the CO_2 feature to greater than 3σ confidence with three to four transits. When decreasing the CO_2 abundance to 1 ppm it takes nine transits

to detect the CO_2 feature to $\sim 3\sigma$. We plot the sigma detection of CO_2 as a function of transit observations, and the corresponding Gaussian feature model, for each scenario in Fig. 7. We performed the same test for NIRISS/SOSS and found that it is not possible to detect, to 3σ, the 1 bar N_2 atmosphere with 1ppm CO_2. We found that it would take 10 transits to detect the 1 bar N_2 atmosphere with 1000ppm CO_2 to 3σ.

6 CONCLUSIONS

In this paper, we present the first atmospheric observation of the super-Earth GJ 357 b. We observed a single transit using NIRISS/SOSS as part of the NEAT GTO programme. Despite obtaining only a partial transit (we missed the first ~ 40 per cent of the transit), we still recover a transmission spectrum to analyse.

We explored whether we could detect any spectral features using a Gaussian feature analysis but find that the Gaussian model is disfavoured compared to a flat line model with the precision we achieve. We also do not find any statistically significant evidence for stellar contamination in our transmission spectrum despite the late type of the host star. We then model a range of atmospheric scenarios as a function of metallicity and cloud top pressure. We find that we can reject atmospheres lighter than $100\times$ solar metallicity, with clouds at pressures >0.01 bar (see Fig. 3). Further observations would be able to determine if heavier atmospheres are present and break the degeneracy between atmospheric metallicity and cloud top pressure. We model the bulk interior composition of the planet using a three-layered model (iron core, silicate mantle, water layer) and find that the interior is consistent with an Earth-like composition.

We argued that GJ 357 b is a relatively good candidate for having retained a secondary atmosphere, such as dominated by CO_2, which could be elucidated with the NIRSpec/G395H observations from the COMPASS survey. The secondary atmosphere of a cool, $\sim 2M_\oplus$ super-Earth orbiting an exceptionally quiescent Mid-M star (M2.5V) is expected to be protected from bulk escape on the main sequence (Chatterjee & Pierrehumbert 2024) and may be optimal for replenishment by volcanism after the active pre-main-sequence phase of volatile loss (Dorn et al. 2018). The major uncertainties are the time spent in an energetic flaring state (e.g. France et al. 2020) and the extent of volatile depletion in the mantle on entering the main sequence (e.g. Krissansen-Totton et al. 2024). Furthermore, modelling of evolution scenarios for the GJ 357 would benefit from follow-up X-ray measurements, such as with *XMM–Newton*.

Finally, we predict the ability to detect an atmosphere using MIRI/LRS and/or MIRI photometry. We find that we can determine if the flux deviates from a blackbody with two eclipse measurements with MIRI/LRS or with a number of photometric filters, but these results would be degenerate between a reflective surface and an atmosphere. Transmission spectra can break this degeneracy, therefore, we compute transmission spectra based on these simulations and show that they are consistent with the current observations, we cannot rule them out. We simulated the ability to detect an atmosphere in transmission using NIRSpec/G395H, with a focus on the 4.3 μm CO_2 feature. We find that, with three to four transit observations, it would be possible to detect a 1 bar N_2 atmosphere with 1000 ppm of CO_2. Our analysis demonstrates the favourability to observe GJ 357b in both transmission and emission with *JWST*.

ACKNOWLEDGEMENTS

The authors thank the anonymous reviewer for their helpful feedback which improved the clarity of our analysis and manuscript. The authors thank Darius Modirrousta-Galian and Ignazio Pillitteri for help with interpreting the *XMM–Newton* observations. We thank Claire Guimond and Raymond Pierrehumbert for feedback on the initial manuscript which greatly improved our clarity. JT was supported by the Glasstone Benefaction, University of Oxford (Violette and Samuel Glasstone Research Fellowships in Science 2024). MR would like to acknowledge funding from the Natural Sciences and Research Council of Canada (NSERC), as well as from the Fonds de Recherche du Québec–Nature et Technologies (FRQNT). This project was undertaken with the financial support of the Canadian Space Agency. This project has been carried out within the framework of the National Centre of Competence in Research PlanetS supported by the Swiss National Science Foundation under grant 51NF40_205606. SP acknowledges the financial support of the SNSF. LD is a Banting and Trottier Post-doctoral Fellow and acknowledges support from NSERC and the Trottier Family Foundation. DJ was supported by NRC Canada and by an NSERC Discovery Grant. NBC acknowledges support from an NSERC Discovery Grant, a Tier 2 Canada Research Chair, and an Arthur B. McDonald Fellowship. The authors also thank the Trottier Space Institute and l'Institut de recherche sur les exoplanètes for their financial support and dynamic intellectual environment. This work is based on observations made with the NASA/ESA/CSA *JWST*. RDC acknowledges support from the Science and Technology Facilities Council (STFC) and the Alfred P. Sloan Foundation under grant G202114194 (AEThER). The data were obtained from the Mikulski Archive for Space Telescopes at the Space Telescope Science Institute, which is operated by the Association of Universities for Research in Astronomy, Inc., under NASA contract NAS 5–03127 for *JWST*. The specific observations analysed can be accessed via DOI 10.17909/zq0q-jd03. This research has made use of the NASA Exoplanet Archive, which is operated by the California Institute of Technology, under contract with the National Aeronautics and Space Administration under the Exoplanet Exploration Program. This publication makes use of The Data & Analysis Center for Exoplanets (DACE), which is a facility based at the University of Geneva (CH) dedicated to extrasolar planets data visualization, exchange and analysis. DACE is a platform of the Swiss National Centre of Competence in Research (NCCR) PlanetS, federating the Swiss expertise in Exoplanet research. The DACE platform is available at https://dace.unige.ch.

DATA AVAILABILITY

The data are available upon request.

REFERENCES

Alam M. K. et al., 2024, AJ, 169, 15
Albert L. et al., 2023, PASP, 135, 075001
Alderson L. et al., 2024, AJ, 167, 216
Alderson L. et al., 2025, AJ, 169, 142
Asplund M., Grevesse N., Sauval A. J., Scott P., 2009, ARA&A, 47, 481
Banerjee A. et al., 2024, ApJ, 975, L11
Barber R. J., Strange J. K., Hill C., Polyansky O. L., Mellau G. C., Yurchenko S. N., Tennyson J., 2014, MNRAS, 437, 1828
Batalha N. E. et al., 2017, PASP, 129, 064501
Benneke B. et al., 2024, JWST Reveals CH_4, CO_2, and H_2O in a Metal-rich Miscible Atmosphere on a Two-Earth-Radius Exoplanet
Boro Saikia S. et al., 2018, A&A, 616, A108
Buchner J. et al., 2014, A&A, 564, A125
Cadieux C. et al., 2024, ApJ, 970, L2
Canto J., Raga A. C., 1991, ApJ, 372, 646

Chatterjee R. D., Pierrehumbert R. T., 2024, Novel Physics of Escaping Secondary Atmospheres May Shape the Cosmic Shoreline, preprint (arXiv:2412.05188)
Cloutier R. et al., 2017, A&A, 608, A35
Cloutier R. et al., 2019, A&A, 621, A49
Cohen O., Glocer A., Garraffo C., Alvarado-Gómez J. D., Drake J. J., Monsch K., Puigdomenech F. F., 2024, ApJ, 962, 157
Coles P. A., Yurchenko S. N., Tennyson J., 2019, MNRAS, 490, 4638
Coulombe L.-P. et al., 2023, Nature, 620, 292
Coulombe L.-P. et al., 2025, preprint (arXiv:2501.14016)
Damiano M. et al., 2022, AJ, 164, 225
Darveau-Bernier A. et al., 2022, PASP, 134, 094502
de Wit J. et al., 2016, Nature, 537, 69
de Wit J. et al., 2018, Nat. Astron., 2, 214
Diamond-Lowe H. et al., 2024, A&A, 689, A48
Dong C., Jin M., Lingam M., Airapetian V. S., Ma Y., van der Holst B., 2018, Proc. Natl. Acad. Sci., 115, 260
Dorn C., Venturini J., Khan A., Heng K., Alibert Y., Helled R., Rivoldini A., Benz W., 2017a, A&A, 597, A37
Dorn C., Hinkel N. R., Venturini J., 2017b, A&A, 597, A38
Dorn C., Noack L., Rozel A. B., 2018, A&A, 614, A18
Doyon R. et al., 2023, PASP, 135, 098001
Dressing C. D., Charbonneau D., 2015, ApJ, 807, 45
Engle S. G., 2023, ApJ, 960, 62
Espinoza N., Kossakowski D., Brahm R., 2019, MNRAS, 490, 2262
Feinstein A. D. et al., 2023, Nature, 614, 670
Foreman-Mackey D., Agol E., Ambikasaran S., Angus R., 2017, AJ, 154, 220
Fournier-Tondreau M. et al., 2024, MNRAS, 528, 3354
France K. et al., 2020, AJ, 160, 237
Freedman R. S., Lustig-Yaeger J., Fortney J. J., Lupu R. E., Marley M. S., Lodders K., 2014, ApJS, 214, 25
Garcia L. J., Moran S. E., Rackham B. V., Wakeford H. R., Gillon M., de Wit J., Lewis N. K., 2022, A&A, 665, A19
Gillon M. et al., 2016, Nature, 533, 221
Gillon M. et al., 2017, Nature, 542, 456
Grant D., Wakeford H. R., 2024, J. Open Source Softw., 9, 6816
Greene T. P., Bell T. J., Ducrot E., Dyrek A., Lagage P.-O., Fortney J. J., 2023, Nature, 618, 39
Gregory P., 2005, Bayesian Logical Data Analysis for the Physical Sciences: A Comparative Approach with Mathematica®Support. Cambridge Univ. Press, Cambridge, Cambridge
Gressier A. et al., 2024a, ApJ, 975, L10
Gressier A. et al., 2024b, JWST-TST DREAMS: A Super-Solar Metallicity in WASP-17 b Dayside Atmosphere from NIRISS SOSS Eclipse Spectroscopy
Guimond C. M., Wang H., Seidler F., Sossi P., Mahajan A., Shorttle O., 2024, Rev. Mineral. Geochem., 90, 259
Hakim K., Rivoldini A., Van Hoolst T., Cottenier S., Jaeken J., Chust T., Steinle-Neumann G., 2018, Icarus, 313, 61
Haldemann J., Dorn C., Venturini J., Alibert Y., Benz W., 2024, A&A, 681, A96
Hammond M. et al., 2024, Reliable Detections of Atmospheres on Rocky Exoplanets with Photometric JWST Phase Curves
Hirose K., Wood B., Vočadlo L., 2021, NREE, 2, 645
Ho C. S. K., Rogers J. G., Van Eylen V., Owen J. E., Schlichting H. E., 2024, MNRAS, 531, 3698
Hu R., Ehlmann B. L., Seager S., 2012, ApJ, 752, 7
Huang C., Rice D. R., Steffen J. H., 2022, MNRAS, stac1133
Husser T.-O., Berg S. W.-v., Dreizler S., Homeier D., Reiners A., Barman T., Hauschildt P. H., 2013, A&A, 553, A6
Ih J., Kempton E. M.-R., Whittaker E. A., Lessard M., 2023, ApJ, 952, L4
JWST Transiting Exoplanet Community Early Release Science Team, 2023, Nature, 614, 649
Jenkins J. S., Pozuelos F. J., Tuomi M., Berdiñas Z. M., Díaz M. R., Vines J. I., Suárez J. C., Peña Rojas P. A., 2019, MNRAS, 490, 5585
Ji X., Chatterjee R. D., Park Coy B., Kite E. S., 2025, preprint (arXiv:2504.19872)
Johnstone C. P., Bartel M., Güdel M., 2021, A&A, 649, A96
Kallinger T. et al., 2014, A&A, 570, A41
Kipping D. M., 2013, MNRAS, 435, 2152
Kirk J. et al., 2024, AJ, 167, 90
Kite E. S., Barnett M. N., 2020, PNAS
Koll D. D. B., Malik M., Mansfield M., Kempton E. M. R., Kite E., Abbot D., Bean J. L., 2019, ApJ, 886, 140
Kreidberg L., 2015, PASP, 127, 1161
Krissansen-Totton J., Wogan N., Thompson M., Fortney J. J., 2024, Nat. Commun., 15, 8374
Lim O. et al., 2023, ApJ, 955, L22
Lincowski A. P. et al., 2023, ApJ, 955, L7
Line M. R. et al., 2013, ApJ, 775, 137
Luger R., Lustig-Yaeger J., Agol E., 2017, ApJ, 851, 94
Luque R. et al., 2019, A&A, 628, A39
Lustig-Yaeger J. et al., 2023, Nat. Astron., 7, 1317
MacDonald R. J., 2023, J. Open Source Softw., 8, 4873
Magic Z., Chiavassa A., Collet R., Asplund M., 2015, A&A, 573, A90
Mansfield M., Kite E. S., Hu R., Koll D. D. B., Malik M., Bean J. L., Kempton E. M. R., 2019, ApJ, 886, 141
Mansfield M. W. et al., 2024, No Thick Atmosphere on the Terrestrial Exoplanet Gl 486b
Marvin C. J., Reiners A., Anglada-Escudé G., Jeffers S. V., Boro Saikia S., 2023, A&A, 671, A162
May E. M. et al., 2023, ApJ, 959, L9
Modirrousta-Galian D., Stelzer B., Magaudda E., Maldonado J., Güdel M., Sanz-Forcada J., Edwards B., Micela G., 2020, A&A, 641, A113
Moran S. E. et al., 2023, ApJ, 948, L11
Nakayama A., Ikoma M., Terada N., 2022, ApJ, 937, 72
Oddo D. et al., 2023, AJ, 165, 134
Parker E. N., 1958, ApJ, 128
Patel J. A., Espinoza N., 2022, AJ, 163, 228
Penz T., Micela G., 2008, A&A, 479, 579
Pereira F. et al., 2019, MNRAS, 489, 5764
Piaulet-Ghorayeb C. et al., 2024, ApJ, 974, L10
Polyansky O. L., Kyuberis A. A., Zobov N. F., Tennyson J., Yurchenko S. N., Lodi L., 2018, MNRAS, 480, 2597
Pont F., Knutson H., Gilliland R. L., Moutou C., Charbonneau D., 2008, MNRAS, 385, 109
Rackham B. V., Apai D., Giampapa M. S., 2018, ApJ, 853, 122
Rackham B. V., Apai D., Giampapa M. S., 2019, AJ, 157, 96
Radica M., 2024, J. Open Source Softw., 9, 6898
Radica M. et al., 2022a, PASP, 134, 104502
Radica M. et al., 2022b, MNRAS, 517, 5050
Radica M. et al., 2023, MNRAS, 524, 835
Radica M. et al., 2024, ApJ, 962, L20
Radica M. et al., 2025, ApJ, 979, L5
Redfield S. et al., 2024, Report of the Working Group on Strategic Exoplanet Initiatives with HST and JWST
Richard C. et al., 2012, J. Quant. Spectrosc. Radiat. Transf., 113, 1276
Robinson T. D., Catling D. C., 2014, Nature Geoscience, 7, 12
Rogers L. A., Seager S., 2010, ApJ, 712, 974
Rogers J. G., Gupta A., Owen J. E., Schlichting H. E., 2021, MNRAS, 508, 5886
Rothman L. S. et al., 2010, J. Quant. Spectrosc. Radiat. Transf., 111, 2139
STScI Development Team, 2013, Astrophysics Source Code Library, record ascl:1303.023
Scarsdale N. et al., 2024, JWST COMPASS: The 3–5 Micron Transmission Spectrum of the Super-Earth L 98–59 c,
Schlawin E. et al., 2024, ApJ, 974, L33
Seager S., Deming D., 2009, ApJ, 703, 1884
Seager S., Mallen-Ornelas G., 2003, ApJ, 585, 1038
Sotin C., Grasset O., Mocquet A., 2007, Icarus, 191, 337
Spaargaren R. J., Wang H. S., Mojzsis S. J., Ballmer M. D., Tackley P. J., 2023, ApJ, 948, 53
Stock J. W., Kitzmann D., Patzer A. B. C., 2022, MNRAS, 517, 4070
Taylor J., 2025, RNAAS, 9, 118
Taylor J. et al., 2023, MNRAS, 524, 817

Trotta R., 2008, Contemp. Phys., 49, 71
Unterborn C. T., Dismukes E. E., Panero W. R., 2015, ApJ, 819, 32
Unterborn C. T., Foley B. J., Desch S. J., Young P. A., Vance G., Chiffelle L., Kane S. R., 2022, ApJ, 930, L6
Wakeford H. R. et al., 2019, AJ, 157, 11
Watson A. J., Donahue T. M., Ker J. C. G. W., 1981, Icarus, 48, 150
Wood B. E. et al., 2021, ApJ, 915, 37
Zahnle K. J., Catling D. C., 2017, ApJ, 843, 122
Zhou L., Ma B., Wang Y.-H., Zhu Y.-N., 2023, Res. Astron. Astrophys., 23, 025011
Zieba S. et al., 2023, Nature, 620, 746

APPENDIX A: EXPLORING THE C/O DEPENDENCE

We perform an atmospheric retrieval with the set-up described in Section 3.3. We have five free parameters: metallicity with priors [–1,4] in log-space, C/O ratio with priors [0,1] in linear-space, planet-radius scaling factor with priors [0.8,1.2] in linear space, cloud top pressure with priors [–6,2] in log-space, and temperature with priors [300,800] in linear-space. We plot the best-fitting range of spectra and posterior distribution of the metallicity versus C/O in Fig. A1. We find that there is no dependence on the C/O ratio.

APPENDIX B: ADDITIONAL FIGURES AND TABLE

Fig. B1 shows a comparison between the NIRISS/SOSS GJ 357 b transmission that we obtain with and without cutting integrations affected by correlated noise.

Fig. B2 shows the best-fitting limb-darkening values from our spectroscopic fits, compared to stellar models

Table B1 has the `exoTEDRF` transmission spectrum used in this work.

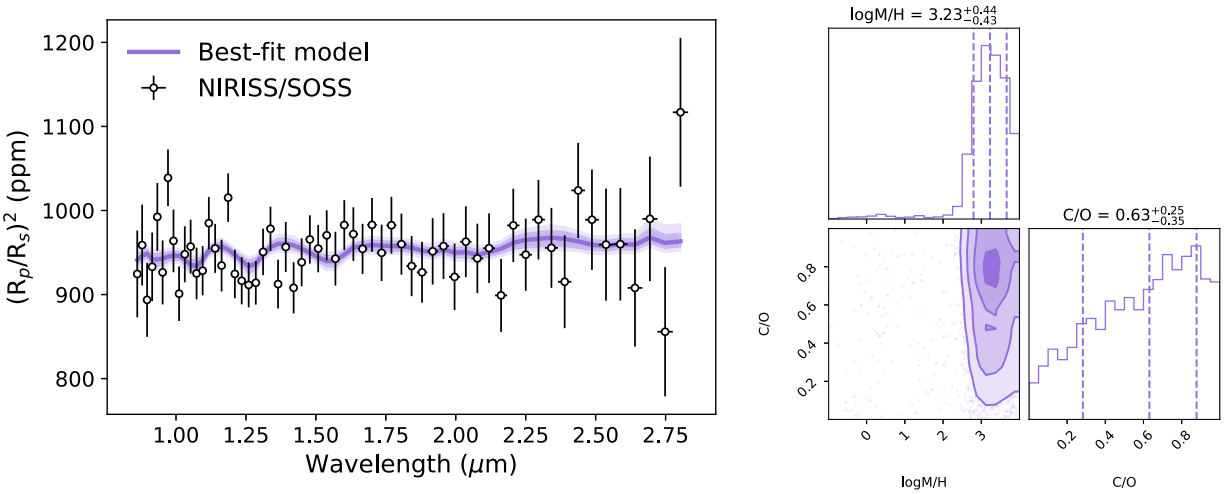

Figure A1. Best-fitting models and posterior distributions of the metallicity and C/O ratio from a simple atmospheric retrieval based on the model described in Section 3.3. We show that the atmospheric inferences has no dependence on the C/O ratio.

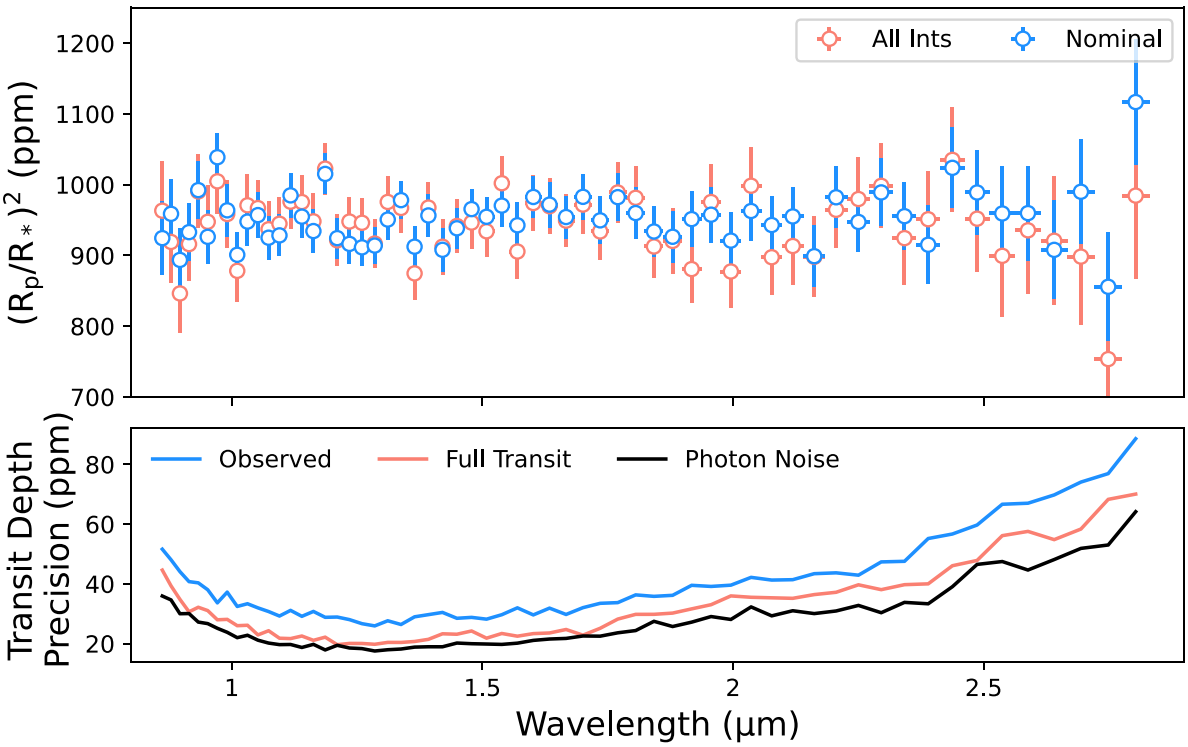

Figure B1. *Top*: comparison of our nominal NIRISS/SOSS transmission spectrum of GJ 357 b (blue), obtained cutting the ∼500 integrations after transit egress most affected by uncorrectable correlated noise during the light curve fits, and the transmission spectrum obtained by including all integrations in the fit (red). *Bottom*: effects of observing only a partial transit on the achieved transit depth precision. Our observed precision (blue) is compared to the precision that we would have achieved if the full transit was observed (red) and the photon-noise precision (black).

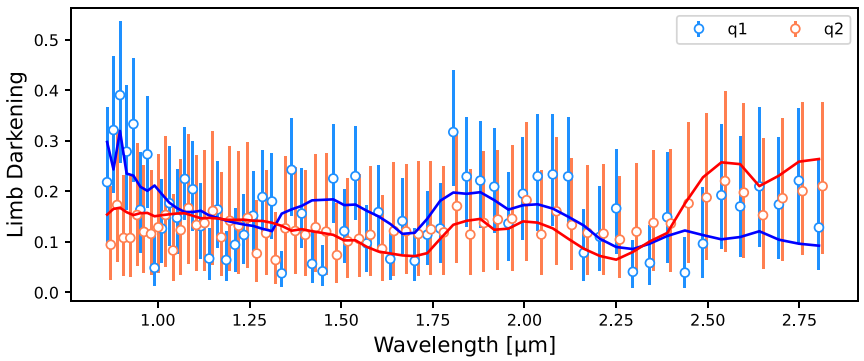

Figure B2. Best-fitting quadratic limb-darkening values as a function of wavelength (points with error bars), compared to `ExoTiC-LD` predictions (solid lines) using 3D Stagger stellar models. Points are slightly offset in wavelength space for visual clarity.

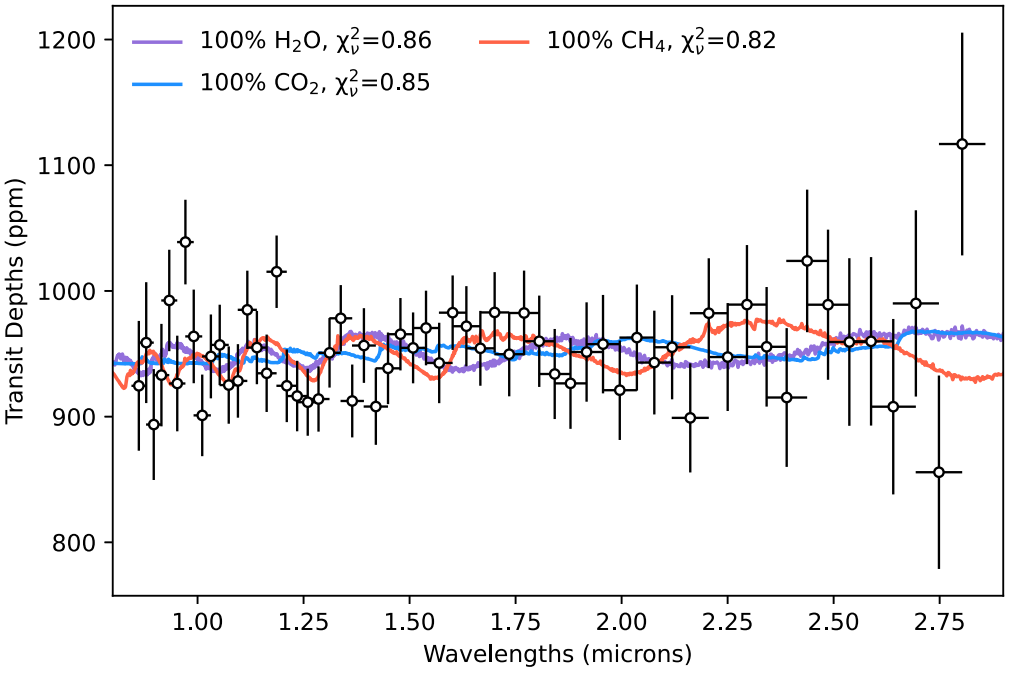

Figure B3. Transmission spectrum of GJ 357 b with three atmospheric models overplotted. The reduced χ^2 for each model is quoted in the legend. We show three 'end-member' models: pure-H_2O, pure-CO_2, and pure-CH_4.

Table B1. `exoTEDRF` transmission spectrum of GJ 357 b used in this work.

Wavelength (μm)	Wavelength error (μm)	Transit depth (ppm)	Transit depth error (ppm)
0.862	0.009	924.53	51.62
0.879	0.009	958.87	48.08
0.897	0.009	893.72	44.12
0.915	0.009	933.02	40.77
0.933	0.009	992.42	40.35
0.952	0.010	926.36	38.04
0.971	0.010	1038.87	33.66
0.991	0.010	963.82	37.24
1.011	0.010	901.00	32.46
1.031	0.010	947.91	33.36
1.052	0.011	957.06	31.98
1.074	0.011	925.11	30.75
1.095	0.011	928.41	29.24
1.117	0.011	984.98	31.14
1.140	0.011	954.93	29.15
1.163	0.012	934.49	30.78
1.186	0.012	1015.27	28.81
1.210	0.012	924.54	28.91
1.235	0.012	916.39	28.04
1.260	0.013	911.47	26.68
1.285	0.013	914.01	25.94
1.311	0.013	950.78	27.66
1.338	0.013	978.23	26.41
1.365	0.014	912.46	28.98
1.392	0.014	956.57	29.71
1.420	0.014	908.03	30.45
1.449	0.014	938.43	28.49
1.478	0.015	965.56	28.80
1.508	0.015	954.70	28.20
1.539	0.015	970.51	29.69
1.570	0.016	942.70	31.99
1.602	0.016	982.71	29.62
1.634	0.016	971.91	31.89
1.667	0.017	954.35	29.77
1.701	0.017	982.90	32.05
1.735	0.017	949.66	33.50
1.770	0.018	982.45	33.73
1.806	0.018	959.96	36.32
1.842	0.018	933.92	35.83
1.879	0.019	926.47	36.18
1.917	0.019	951.41	39.53
1.956	0.020	957.67	39.15
1.996	0.020	921.03	39.58
2.036	0.020	962.88	42.19
2.077	0.021	943.02	41.28
2.119	0.021	955.20	41.41
2.162	0.022	899.02	43.42
2.206	0.022	982.27	43.71
2.250	0.023	947.40	42.92
2.296	0.023	989.12	47.37
2.342	0.023	955.55	47.56
2.389	0.024	915.21	55.19
2.438	0.024	1023.87	56.71
2.487	0.025	989.04	59.71
2.537	0.025	959.37	66.67
2.588	0.026	959.90	67.01
2.641	0.026	907.92	69.79
2.694	0.027	990.07	74.10
2.748	0.027	855.77	76.93
2.803	0.027	1116.87	88.60

This paper has been typeset from a TEX/LATEX file prepared by the author.